

A Novel Approach for Temporal Discretizations with High-order Finite Volume Schemes

Pedro Miguel Pereira Costa
pedro.m.p.costa@tecnico.ulisboa.pt

Instituto Superior Técnico, Universidade de Lisboa, Portugal

November 2019

Abstract

With the finite volume method (FVM), the temporal term of the equation must be integrated in space with the same accuracy order as the convection and diffusion schemes. One classic way to solve this issue is to consider average computational values in FVM. Another approach is to consider a new operator that converts pointwise values to mean ones, which enables high-order convection and diffusion schemes of the pointwise framework in unsteady problems. One advantage of these schemes is the low number of contributions to the coefficient matrix when compared to the mean-value counterpart. In the 2D space, this mean operator uses the weighted least-squares method to compute local polynomials and the Gauss quadrature to integrate cell inertial momentums (up to the desired order). The code was verified for fourth, sixth and eighth orders in both Cartesian and unstructured meshes when using the Crank-Nicolson time discretization. Dirichlet and Neumann boundary conditions were also successfully verified. Additionally, the numerical spatial error evolution with the solver runtime and the required memory are studied as efficiency metrics of the implemented high-order schemes. High-order spatial schemes provided faster and more accurate results than the second-order counterpart. To reduce the number of required time steps, high-order backward differentiation formula (BDF) schemes were verified and lead to considerable time savings when using high-order spatial schemes.

Keywords: High-order schemes, Transient simulations, Finite volume method, Weighted least-squares, Polyhedral unstructured grids, Backward differentiation formulas.

1. Introduction

CFD has always been strongly steered by the evolution of modern computers when it comes to faster computing, larger memory or in the way numerical algorithms are designed, for example, its possibility to be parallelized [1]. Therefore, in the nineties with increases of the computers' speed and memory capacity, it was possible to perform simulations using Reynolds averaged Navier-Stokes (RANS) equations.

Until today, RANS is essentially limited to steady attached flows. NASA CFD Vision 2030 Study (2014) [2] also states that the current methods are still unable to predict turbulent-separated flows. RANS cannot predict reliably separated and unsteady flow phenomena such as buffet. So wind tunnel testing is still cheaper than a very large number of RANS calculations [3].

Vector computers changed the paradigm of CFD in the eighties as the number of flops per second increased drastically and kept gradually improving. However, in the early 2000s the bandwidth did not

keep up its rate and it is seen as a major issue nowadays to overcome [4]. LES simulations require exascale computing to design a whole aircraft's fuselage [5]. Although some hybrid RANS-LES methods are commonly used in simulations where swirls and intentionally detached flows are present, methods combining near wall RANS and far field LES are still in its infancy [2].

Especially as most computation time is spent solving the equations near-wall designing new numerical methods such as higher-order schemes may be an option to reduce the number of flops in a simulation increasing its speed.

2. Background

Solving convection-diffusion equations using Finite Volume (FV) methods was introduced in the sixties by Tikhonov and Samarskii [6] and revived in the eighties by Patankar [7]. Barth and Frederikson (1990) [8] introduced a quadratic reconstruction to solve Euler equations and more recent efforts led to schemes up to fourth-order by Ollivier-Gooch

et al. [9] and sixth-order schemes on unstructured grids by Clain *et al.* [10]. A comparison study by Nogueira *et al.* [11] showed that, for the same accuracy level, FV schemes require four times less degrees of freedom than its finite element method counterpart when solving the Navier-Stokes equations. To avoid oscillations near discontinuities more recent techniques such as essentially non-oscillatory (ENO) [12] and weighted essentially non-oscillatory (WENO) [13] were developed for high-order schemes. Ollivier-Gooch *et al.* [14] used a fourth-order FV scheme to solve a flow around a NACA 0012 airfoil, which showed improvements in accuracy and Jalali *et al.* [15] presented another one for highly-anisotropic grids, which can be used in simulations for turbulent boundary layers.

The present work expands on the results of Vasconcelos [16] and Diogo [17], who developed convection-diffusion schemes (up to eighth-order) for steady cases on unstructured grids.

Backward Differentiation Formulas (BDF) schemes are high-order temporal schemes, which were first mentioned by Curtis and Hirschfelder (1952) [18]. These schemes were dismissed by Farnell (1962) [19] as they were less accurate than Adams-Moulton [20], which is true for non-stiff equations. BDF schemes up to sixth-order are stable for stiff problems and allow larger timesteps than explicit schemes. BDF2 is L-stable and very popular, it is even used in software such as COMSOL. BDF3 is not A-stable and it performs inconsistently [21]. Therefore extended BDF (EBDF) [22] and modified EBDF (MEBDF) [23] were developed and they are A-stable up to fourth-order. The two implicit advanced step-point (TIAS) method is A-stable up to sixth-order [24].

3. Proposed Schemes

Unstructured grids are useful to compute flows along complex boundaries or when discretizing local grid refinements with smooth grid size. When building the mean operator, the weighted least-squares is used to minimize the interpolation error of the local polynomials using the correspondent values of the cell neighbours and from face boundaries when needed.

Reference length is used as spatial parameter such that:

$$H = \sqrt{\frac{\text{Domain Area}}{n_{\text{cells}}}} \quad (1)$$

which in Cartesian grids reverts to the cell face's length and the discretized domain is a square of one per one (meter).

The general transport equation considered is

$$\frac{\partial \phi}{\partial t} = \nabla \cdot (\Gamma \nabla \phi) - \nabla \cdot (U \phi) + \varphi_\phi \quad (2)$$

where ϕ is the transported value, U is the convection velocity and Γ is the diffusion coefficient and φ_ϕ is the source term.

Integrating both sides in time and space using the Control Volume:

$$\underbrace{\int_t \int_{CV} \frac{\partial \phi}{\partial t} dV dt}_{\text{Transient Term}} = \int_t \int_{CV} \left(\underbrace{\nabla \cdot (\Gamma \nabla \phi)}_{\text{Diffusive Term}} - \underbrace{\nabla \cdot (U \phi)}_{\text{Convective Term}} + \underbrace{\varphi_\phi}_{\text{Source Term}} \right) dV dt \quad (3)$$

Since the convection and diffusion terms were explained in the work of Vasconcelos [16] and Diogo [17], high-order convection-diffusion schemes are here reduced to the matrix A .

When discretizing the global equation with CN time scheme leads to:

$$\begin{aligned} (V_p M - 0.5 \Delta t A) \phi^{n+1} = \\ (V_p M + 0.5 \Delta t A) \phi^n + 0.5 \Delta t (S^{n+1} + S^n) \end{aligned} \quad (4)$$

where A is the matrix related to the convection and diffusion terms and S is the source term.

In this pointwise framework mean operator only needs to be considered for high-order spatial schemes with an order higher than two.

3.1. Stencil

In unstructured grids the stencil becomes less straightforward than for Cartesian grids and plays therefore a more significant role. A more compact stencil leads to less memory storage and consequently less algebraic computations per timestep. In the 2D case, the n -th spatial accuracy order local polynomial interpolation is given by:

$$\phi_C^R(x, y) = \sum_{i=0}^{n-1} \sum_{j=0}^{n-1} C_k (x - x_C)^i (y - y_C)^j \quad (5)$$

and the mean value is given by:

$$\bar{\phi}_C(x, y) = \frac{1}{V_C} \int_{CV} \phi dV = \frac{1}{V_C} \sum_{i=0}^{n-1} \sum_{j=0}^{n-1} C_k \widehat{x^i y^j} \quad (6)$$

where $\widehat{x^i y^j} = \int_{CV} (x - x_C)^i (y - y_C)^j$ The minimum number of polynomial terms for each spatial order n is $\frac{n(n+1)}{2}$, which is presented in table 1.

Accuracy Order	4	6	8
Number of Terms	10	21	36

Table 1: Number of interpolation terms demanded by each n -th spatial order for the 2D case.

To create a compact stencil the closest cells to cell C must be considered for the reconstruction according to the desired order. For second order only the face neighbours of cell C are considered i.e. cells with a face in common with cell C. For fourth-order schemes the face neighbours and their face neighbours are considered and so forth. It is depicted in figure 1. For each successive even order, a new set of face neighbours is added to the stencil. So that the fourth-order scheme uses up to second-order face neighbours of cell C, the sixth-order scheme uses up to third-order face neighbours and finally the eighth-order one uses up to fourth-order face neighbours. An example of these different types of face neighbours is shown in figure 1 for an irregular polyhedral grid.

The mean operator is built with respect to cells' centroids and boundary faces' centroids. To keep accuracy order stencil's size must be at least as large as the number of terms indicated in table 1 and the number of neighbours across both 2D directions (x and y) must include at least n cell neighbours in each coordinate. When these requirements are not met the stencil must be extended towards within the domain (see Diogo [17]).

Figure 1 shows the stencils used in a local reconstruction for cell C up to eighth-order schemes.

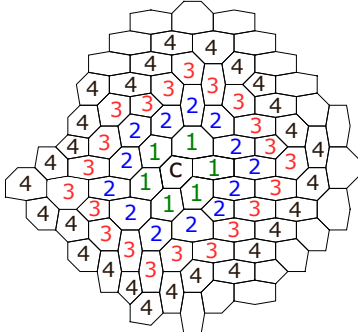


Figure 1: Face neighbours of cell C that are used to compute pointwise-to-mean value conversion operator

3.2. Local Polynomial Reconstructions

The n-th order local reconstruction around cell C using its face neighbours and power expansion leads to the matrix system $D_C c_C = \phi_s$, where c_C stores the local reconstruction coefficients, D_C is $[1, (x - x_C), (y - y_C), \dots]$ and (x, y) are the stencil cells' centroids.

This is an overdetermined problem since the number of stencil neighbours is greater than the number of terms to be computed. So, to minimize the weighted residual, WLS is used.

In order to obtain an invertible square matrix on the left side, both sides of the equation are multiplied by $D_C^T W_C$:

$$D_C^T W_C D_C c_C = D_C^T W_C \phi_s \quad (7)$$

where W_C is a weight matrix that uses a weight function given by $(\frac{1}{d_C / \max(d_C)})^6$, which was optimized by Diogo [17] for both the convection and diffusion schemes.

On the left side of the equation there is now a square matrix with rows linearly independent. Therefore it is possible to invert it.

$$c_C = \underbrace{(D_C^T W_C D_C)^{-1}}_{W_{LS}} D_C^T W_C \phi_s \quad (8)$$

The matrix inversion is performed using Gauss Elimination Method. Starting with $[W_{LS}|I]$ an elimination from down to up is performed, obtaining an upper matrix on the left side. Then it is followed by an elimination from up to down leading to a diagonal matrix and finally obtaining $[I|W_{LS}^{-1}]$.

Local Polynomials coefficients can be stored in a rectangular matrix P such that:

$$c_C = P \phi_s \quad (9)$$

for future reference.

3.3. Boundary Treatment

A stencil may have face boundaries and so BC must be applied in the local polynomial reconstruction. Dirichlet BC imposes the analytical value at the face boundaries. The Neumann BC is implemented as the dot product between the imposed gradient flux and the unitary face boundary's normal pointing outwards the domain. Dirichlet BC implies adding a line to matrix D_C such as $[1, (x_f - x_C), (y_f - y_C), \dots]$. Neumann BC implies adding such as

$$[0, n_x, n_y, 2(x - x_f)n_x, (y_{n_f} - y_C)n_x + (x_{n_f} - x_C)n_y, 2(y - y_f)n_y, \dots]$$

Two sets of boundary condition were considered in this work: full Dirichlet BC is a set with all boundaries imposed with Dirichlet condition, and mixed BC is a case with a Neumann BC at the east boundary and the remaining ones have a Dirichlet condition.

3.4. Inertial Momentums

Similar to the 1D case the inertial momentum vector is computed using Gauss quadrature integration for the 2D space. As mentioned on equation 6 the 2D inertial momentums are given by:

$$\widehat{x^i y^j} = \int_{CV} (x - x_C)^i (y - y_C)^j \quad (10)$$

When considering cells from unstructured grids, the polygonal cells (with more than three faces) can be split into triangles which use the cell's centroid and the two vertexes of each face.

Overall, the cell's inertial momentum is the sum of the gauss quadrature integrations performed in each triangle.

$$\widehat{x^i y^j} = \sum_{b \in J_{(C)}} \left(S_{\Delta b} \sum_{k \in G_{(\Delta b)}} w_{G(k)} (x_k - x_c)^i (y_k - y_c)^j \right) \quad (11)$$

where $J_{(C)}$ is the set of triangles and Δ_b represents each triangle.

Triangle S_{Δ} is computed by:

$$S_{\Delta} = (\mathbf{x}_2 - \mathbf{x}_1) \times (\mathbf{x}_3 - \mathbf{x}_1) \quad (12)$$

In the 2D Cartesian plane the Gauss quadrature points over a triangle can be computed by equation 13 using the simplex coordinates (s_1, s_2 and s_3) and Gauss quadrature weights (w_G) up to spatial order n . Data can be consulted in [25] and [26].

$$x_k = \begin{bmatrix} s_1 & s_2 & s_3 \end{bmatrix} \begin{bmatrix} x_1 & y_1 \\ x_2 & y_2 \\ x_3 & y_3 \end{bmatrix} \quad (13)$$

It is worth mentioning that purely odd inertial moments such as $\widehat{x}, \widehat{y}, \widehat{x^3}, \widehat{y^3}, \dots$ are equal to zero. In triangular cells using eighth-order, it implies computing less 8 inertial momentums (out of 36) per cell.

3.5. Transport Equation Discretization

The pointwise-to-mean conversion operator for 2D domains is computed such that:

$$\overline{\phi_C} = M_C \phi_s = P_{ij} \widehat{x^i y^j} \phi_s \quad (14)$$

When designing the computational algorithm if a stencil includes a face boundary its polynomial coefficient is stored in a separate matrix, M_f .

$$\overline{\phi_{cells}} = M_{cells} \phi_{cells} + M_f \phi_f \quad (15)$$

Combining global transport equation (see equation 4) with equation 15

$$\begin{aligned} (V_p M_{cells} - 0.5 \Delta t A_{cells}) \phi_{cells}^{n+1} = & (V_p M_{cells} + \\ & 0.5 \Delta t A_{cells}) \phi_{cells}^n + M_f (\phi_f^n - \phi_f^{n+1}) + \\ & 0.5 \Delta t (A_f (\phi_f^n + \phi_f^{n+1}) + S^{n+1} + S^n) \end{aligned} \quad (16)$$

3.6. Unstructured Grids in 2D

In order to study the applicability of the proposed schemes to unstructured grids. It was chosen a set of irregular meshes, such as irregular polyhedral (Figure 3.6), triangular, quadrilateral and hybrid grids. Grids were created changing the orientation

of the cells. Size of each cell is not constant but overall the ratio was kept near to one.

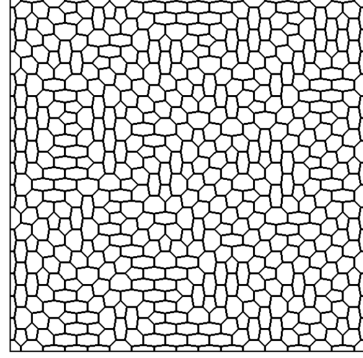


Figure 2: Example of Polyhedral grid (with 545 cells), which was also previously studied by Diogo [17] for steady cases.

4. Transient Results using Crank-Nicolson time discretization

In this section the accuracy order of the mean operator and the transient results with 2D domains will be verified as well as the temporal order. Both full Dirichlet (blue lines) and mixed (red lines) boundary conditions are compared alongside.

Two examples are considered as analytical solutions to the following equation:

$$\begin{aligned} \frac{\partial \phi}{\partial t} + U_x \frac{\partial \phi}{\partial x} + U_y \frac{\partial \phi}{\partial y} = & \Gamma_x \frac{\partial^2 \phi}{\partial x^2} + \Gamma_y \frac{\partial^2 \phi}{\partial y^2} + \varphi_\phi \\ \text{with } U_x, U_y, \Gamma_x, \Gamma_y \in \mathbb{R} \end{aligned} \quad (17)$$

Example 1 - Dampening Cosine (with artificial source $-\varphi_\phi \neq 0$):

$$\begin{aligned} \phi(x, t) = & e^{-t} \cos(3\pi(x + y)), \text{ with source term} \\ \varphi_\phi = & (-1 + 18\pi^2(\Gamma_x + \Gamma_y)) \cos(3\pi(x + y)) \\ & - 3\pi(U_x + U_y) \sin(3\pi(x + y)) \end{aligned} \quad (18)$$

Example 2: Classical Travelling Wave (without any artificial source $-\varphi_\phi = 0$):

$$\phi(x, t) = e^{-(\Gamma_x + \Gamma_y)kk^2\pi^2 t} \sin(kk\pi(x + y + (U_x + U_y)t)) \quad (19)$$

The present results were obtained by setting $U_x = 1, U_y = 1, \Gamma_x = 1$ and $\Gamma_y = 1$ and $kk = 1.2$.

Initially, the pointwise to mean conversion's accuracy order is verified, followed by the Crank-Nicolson temporal order verification and finally the spatial scheme order for Cartesian grids.

4.1. Numerical errors

In order to evaluate the pointwise to mean value conversion using the mean operator, errors are computed comparing the numerical mean value with the analytical mean value such that:

$$e_{mv} = \bar{\phi}_{numerical} - \bar{\phi}_{exact} \quad (20)$$

The numerical error is a sum of discretization scheme error, round-off error and iterative error.

Discretization error, is proportional to scheme's order of accuracy such that

$$e = \phi_{numerical} - \phi_{exact} = O(\Delta x^n, \Delta t^p) \quad (21)$$

where ϕ is the cell value, Δx is the cell's length, Δt is the timestep size, n is the spatial accuracy order and p is the temporal accuracy order.

The global discretization error (mean relative error) is given by the norm,

$$\|e\|_1 = \frac{\sum_{k=1}^{n_{cells}} (|e_k|) / n_{cells}}{\max(|\phi_{exact}|)} \quad (22)$$

The global discretization error is composed by the temporal scheme, the spatial, the round-off and the iterative errors. The error caused by the temporal scheme is dominant when using coarse timesteps. The temporal accuracy order is computed from the slope of the graph curves with:

$$O_p = \frac{\log_{10}(\|e\|_{k+1}) - \log_{10}(\|e\|_k)}{\log_{10}(\Delta t_{k+1}) - \log_{10}(\Delta t_k)} \quad (23)$$

When the global error evolution with the timestep Δt has converged, the spatial error, $\|e_{sp}\|_1$, is obtained as:

$$\|e_{sp}\|_1 = \lim_{\Delta t \rightarrow 0} \|e\|_1 \quad (24)$$

As stopping criteria, the spatial error is equal to the global one, when the timestep refinement leads to less than one percent decrease in global error and spatial accuracy order is given by:

$$O_n = \frac{\log_{10}(\|e_{sp}\|_{k+1}) - \log_{10}(\|e_{sp}\|_k)}{\log_{10}(H_{k+1}) - \log_{10}(H_k)} \quad (25)$$

4.2. Mean Operator

The pointwise to mean conversion must be as accurate as the spatial schemes used for the convection and diffusion schemes. Therefore it is important to verify the mean operator's spatial order before applying it to any transient problem.

Figure 3 shows norm-1 of pointwise to mean value conversion using the mean operator in 2D space with a Cartesian grid. The average order for each spatial scheme is written in bold.

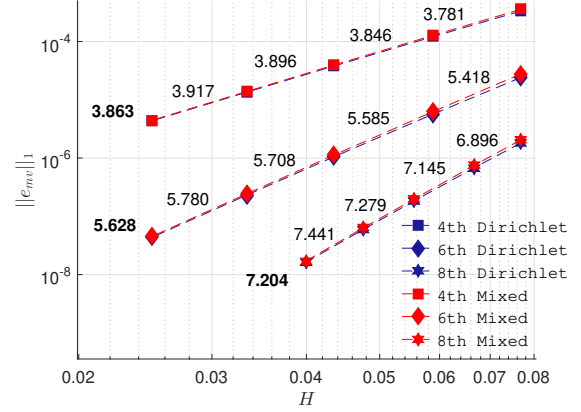


Figure 3: Mean operator error and respective accuracy order with cartesian grids for all high-order schemes using both full Dirichlet and mixed BC cases

For both solutions all curves display a subconvergent behaviour but for each successive refinement the computed order is increasing and tending to the theoretical value. The obtained results when using full Dirichlet and mixed BCs are very similar and curves overlap each other.

4.3. Temporal Discretization

In this section the temporal discretization was done using the Crank-Nicolson time scheme, which is second-order accurate. While the global error is dominated by the temporal error it must decay with the accuracy of the used time scheme.

Figure 4 shows the global error with the timestep size. The eighth-order spatial scheme was used for these results.

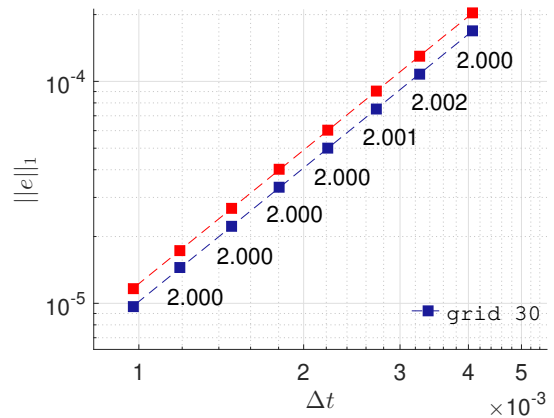


Figure 4: $\|e\|_1$ as a function of timestep size for the eighth-order spatial scheme with Cartesian grids while using CN temporal scheme and for both full Dirichlet and mixed boundary conditions.

For these timesteps the global error is dominated

by the temporal one and the computed order between each timestep refinements is close to the theoretical one.

4.4. Spatial Discretization

When the timestep size is small enough that the global does not change in one percent spatial error is assumed to be obtained.

Figure 5 shows the spatial error decay with H (or cell's length in the Cartesian meshes) considered for these results. The computed order between each successive refinement is shown as well as the average spatial order for each scheme, which is written in bold.

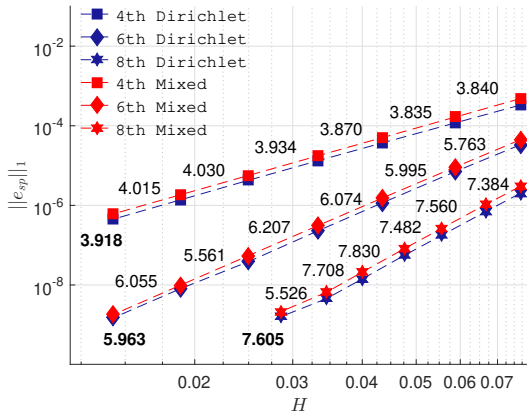


Figure 5: $\|e_{sp}\|_1$ as a function of H with Cartesian grids for all spatial schemes using full Dirichlet and mixed BCs and with the computed order between each mesh refinement.

The computed orders for the Travelling Wave solution are close to their theoretical values. The most refined mesh refinement for the eighth order starts to lose its order due to round-off error.

5. High Order temporal schemes using Cartesian grids

Matrices in 2D spaces have a larger number of non-zeros (NNZ) for the same number of cells due to two dimensions when compared to the 1D case. As a consequence there is a larger amount of algebraic computations per timestep in 2D cases than in 1D ones. Implementing higher-order temporal schemes may allow a lower number of timesteps needed so that global error is only dominated by the spatial error i.e. improving computational time.

The following section aims at verifying high-order BDF schemes and assessing their impact in solver runtime (SRT) when using each high-order spatial scheme. The BDF temporal discretizations (second, fourth and sixth-order) are, respectively:

$$\bar{\phi}^{n+1} - \frac{4}{3}\bar{\phi}^n + \frac{1}{3}\bar{\phi}^{n-1} = \frac{2}{3}\Delta t(A\phi^{n+1} + S^{n+1}) \quad (26)$$

$$\begin{aligned} \bar{\phi}^{n+1} - \frac{48}{25}\bar{\phi}^n + \frac{36}{25}\bar{\phi}^{n-1} - \frac{16}{25}\bar{\phi}^{n-2} + \frac{3}{25}\bar{\phi}^{n-3} \\ = \frac{12}{25}\Delta t(A\phi^{n+1} + S^{n+1}) \end{aligned} \quad (27)$$

$$\begin{aligned} \bar{\phi}^{n+1} - \frac{360}{147}\bar{\phi}^n + \frac{450}{147}\bar{\phi}^{n-1} - \frac{400}{147}\bar{\phi}^{n-2} + \frac{225}{147}\bar{\phi}^{n-3} \\ - \frac{72}{147}\bar{\phi}^{n-4} + \frac{10}{147}\bar{\phi}^{n-5} = \frac{60}{147}\Delta t(A\phi^{n+1} + S^{n+1}) \end{aligned} \quad (28)$$

Results were obtained using Cartesian grids with the MATLAB code.

5.1. Temporal Orders

In order to verify the implemented time schemes the temporal orders for all BDF schemes are verified. When timestep is large enough, the global error is dominated by temporal error and should decay with the theoretical order of the used temporal scheme. Figure 6 shows the global error decay with timestep for BDF2, BDF4 and BDF6 schemes. In all results of this section 5, only Dirichlet BC was considered.

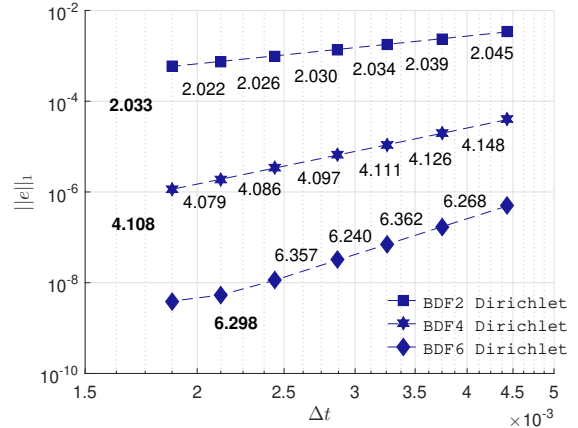


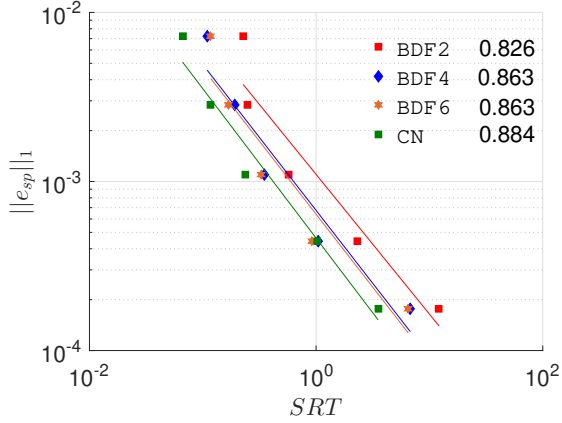
Figure 6: $\|e\|_1$ as function of the timestep for BDF2, BDF4 and BDF6 time schemes for Travelling Wave analytical solution using eighth-order scheme in 2D Cartesian mesh with 30 per 30 cells

The temporal orders are very close to the theoretical ones when using Cartesian grids and an eighth-order spatial scheme. Temporal order should be read when timestep is larger and the spatial error of this analytical case, grid with 30x30 cells and eighth-order scheme is around 4E-9 (see Figure 5). BDF6 starts to flatten for the smallest timesteps as the spatial error's contribution starts to be relevant for the global error.

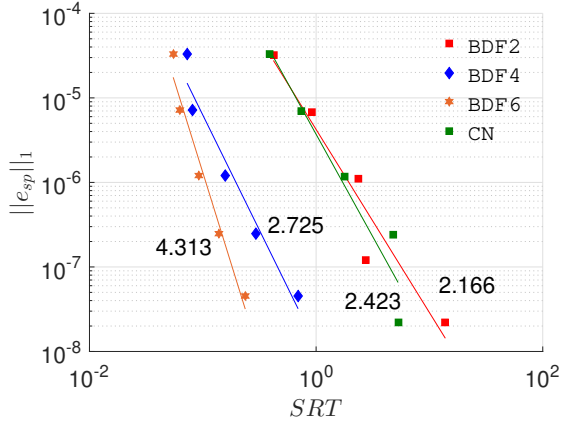
5.2. Solver Runtime

Once the temporal order of each BDF scheme is verified, it is important to perform a comparative study for all spatial schemes using each BDF schemes. The goal is ultimately to assess how fast the high-order temporal schemes provide results.

Figure 7 shows the spatial error decay for second and sixth-order schemes, respectively, using the three BDF schemes introduced and the CN one. Results were obtained solving the Travelling Wave analytical case with Cartesian meshes and only Dirichlet BCs.



(a) 2nd order scheme.



(b) 6th order scheme.

Figure 7: Spatial error evolution with SRT for all temporal and second and sixth-order spatial schemes for the Travelling Wave analytical case

These graphs show how high-order temporal schemes decrease SRT when using high order spatial schemes. For second-order spatial scheme CN provides slightly faster results and the high-order BDF schemes do not provide any relevant improvements when compared with BDF2. For the fourth order spatial scheme BDF4 already shows smaller SRT values than BDF2 and CN. Using BDF6 it leads to slightly faster results than with BDF4 but

with a similar order. For both sixth and eighth spatial schemes BDF6 allows even faster results than the remaining schemes.

Overall all the high-order spatial schemes seem to have an optimal when the temporal scheme is as high-order as possible. However, when the temporal order is lower than the spatial one, there is a noticeable underperformance in terms of efficiency regarding SRT.

For sixth-order schemes, for an error level of E-5 table 2 shows that BDF4 and BDF6 schemes reach time savings up to ninety percent when compared to BDF2 and for error levels of E-7 time savings reach ninety two percent.

$\ e\ _1$	BDF2		BDF4		BDF6	
	SRT (s)	r_1	SRT (s)	r_1	SRT (s)	r_1
E-5	0.6723	1	0.0843	0.1254	0.0624	0.0928
E-7	5.6334	1	0.4567	0.0811	0.1816	0.0322

Table 2: The $\|e\|_1$ estimated for BDF2,BDF4, BDF6 and CN schemes for sixth-order scheme and the respective ratios, using as reference the value from BDF2.

6. Results and Discussion for Unstructured Grids

These results for unstructured grids were obtained using the SOL code. Global system matrix and matrix for explicit multiplication were stored as MSR matrices, explained in AZTEC guide [27], GMRes was used as a linear solver algorithm and the spatial error was obtained when the global error decreased less than one percent with timestep size.

6.1. Spatial Error Orders

High spatial orders were verified by extending the SOL code to transient cases using CN time discretization. It is worth assessing if the proposed schemes are applicable to unstructured grids.

Figure 8 shows the spatial error decay with H for the Dampening Cosine analytical case when using irregular polyhedral meshes (Figure 8) for the three spatial schemes.

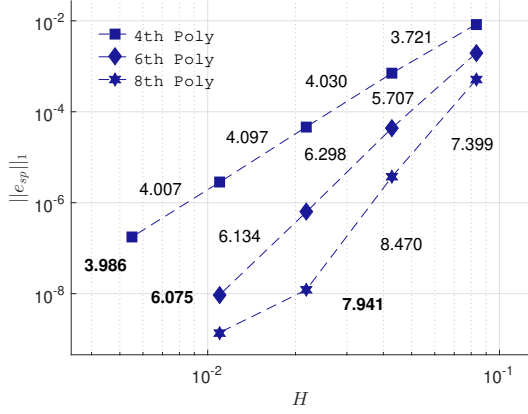


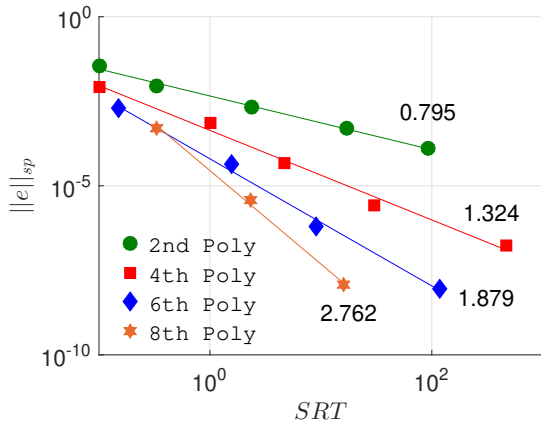
Figure 8: $\|e_{sp}\|_1$ as function of H for the Dampening Cosine analytical case using irregular polyhedral grids, the CN time scheme and only Dirichlet BC in all boundaries.

For the Dampening Cosine solution using an irregular polyhedral mesh curves show a very small overconvergent behaviour for the most refined meshes and the computed average orders are very close to the theoretical ones. The eighth-order scheme for the most refined mesh is affected by round-off and iterative errors.

6.2. Solver Runtime

This subsection evaluates the impact high-order schemes have on SRT when the global error is only dominated by the spatial one. This study aims at assessing which scheme order provides the fastest results for a given error level.

Figure 9 shows the spatial error decay with SRT when using irregular polyhedral meshes for the second and three high-order schemes.



(a) Irregular Polyhedral mesh

Figure 9: $\|e_{sp}\|_1$ as function of SRT for Dampening Cosine analytical case with irregular polyhedral meshes and CN time scheme for the case with only Dirichlet BC.

Using an irregular polyhedral mesh with the sixth-order scheme provides faster results for spatial errors between E-3 and E-4 while the eighth-order is a better option for errors smaller than E-4.

From these results the following equation can be estimated by: $\|e_{sp}\|_1 = O(SRT^{n/2.967})$.

6.3. Memory Storage

When the memory storage is a limiting factor, it is worthwhile studying how the spatial error decays with the total Number of Non-Zeros of the global matrices for each order.

Figure 10 shows the spatial error decay with the Number of Non-Zeros of the global matrices.

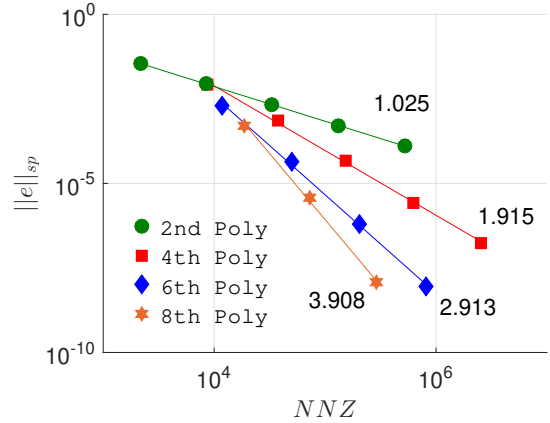


Figure 10: $\|e_{sp}\|_1$ as function of NNZ with irregular polyhedral meshes for Dampening Cosine analytical case using CN time scheme and full Dirichlet BC.

For the irregular polyhedral mesh fourth-order is optimal for errors larger than E-2 regarding memory costs, while sixth-order scheme is the most efficient one for error levels between E-2 and E-4. For errors smaller than E-4, the eighth-order schemes requires less memory than the other ones.

From these results the following equation $\|e_{sp}\|_1 = O(NNZ^{n/2})$ is verified.

7. Grid Topology

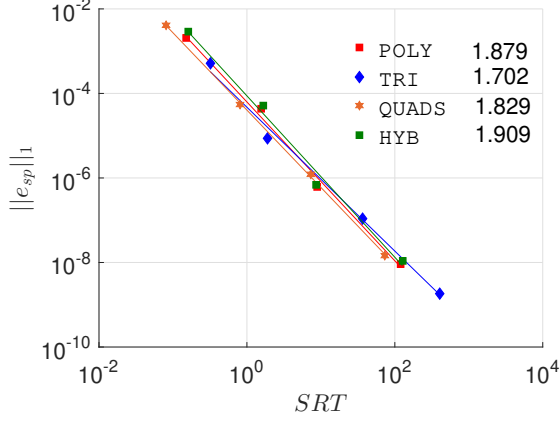
The following comparative study aims at evaluating how the four sets of selected irregular meshes perform regarding SRT and memory storage for the sixth-order scheme.

Figure 11 compares the spatial error evolution with SRT and memory storage when using sixth-order spatial schemes and for all irregular grids at study. Regarding SRT all curves almost overlap each other but the irregular quadrilateral mesh shows time savings of ten percent when compared to triangular meshes when estimating SRT for a spatial error of E-5 from Figure 11(a).

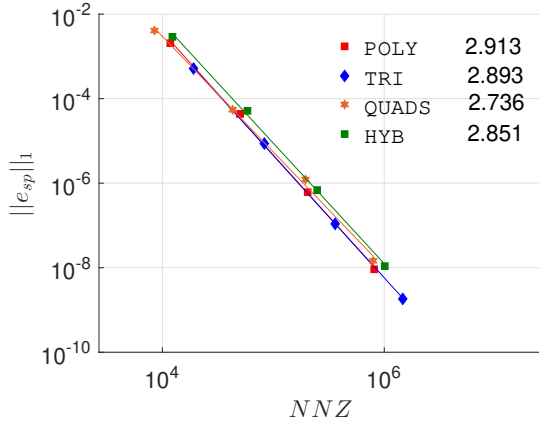
Memory cost results for the irregular triangular mesh are slightly better than the remaining ones.

From 11(b) for a spatial error of E-5 triangular meshes show memory savings of only three percent when compared to quadrilateral meshes.

The hybrid grid as expected can be considered the worst for both criteria (SRT and NNZ), although it has a similar order decay as the other irregular grids have.



(a) Solver Runtime



(b) Memory Storage

Figure 11: $\|e_{sp}\|_1$ as function of SRT and NNZ for sixth-order spatial scheme in the Dampening Cosine analytical case.

8. Conclusions

In the 2D space the local polynomial reconstructions lead to overdetermined matrices. So in order to minimise residual error, the weighted least-squares method was used. The pointwise to mean conversion orders were effectively verified for two analytical solutions before applying the method to transient problems.

The 2D unsteady cases were temporally discretized using Crank-Nicolson method. Numerical temporal orders were close to the theoretical ones. When the timestep is small enough, the global error starts to be dominated by the spatial one. The numerical spatial orders were close to each expected theoreti-

cal value.

High-order BDF schemes were considered for the Travelling Wave analytical case and their temporal orders were effectively verified. When comparing all BDF schemes using each spatial scheme, it was evident that the best results regarding SRT were achieved when BDF6 was used.

Afterwards spatial orders for all schemes were verified for irregular polyhedral meshes for the Dampening Cosine analytical solution.

Regarding both SRT and memory storage case, high-order schemes proved to be advantageous for errors smaller than E-1. Overall fourth-order schemes seem to be the best one for error levels between E-1 and E-3, the fourth-order for error levels between E-3 and E-5, while the eighth-order for even smaller errors.

With sixth-order scheme, irregular quadrilateral meshes showed the fastest SRT, with time savings of ten percent when compared to triangular and polyhedral meshes and of thirty percent when compared to hybrid ones.

References

- [1] Bram Van Leer. CFD education: Past, present, future. In *37th Aerospace Sciences Meeting and Exhibit*, 1999.
- [2] John R. Chawner, John F. Dannenhoffer, and Nigel J. Taylor. Geometry, mesh generation, and the CFD 2030 vision. In *46th AIAA Fluid Dynamics Conference*, 2016.
- [3] F. D. Witherden and A. Jameson. Future directions of computational fluid dynamics. In *23rd AIAA Computational Fluid Dynamics Conference, 2017*, 2017.
- [4] F. D. Witherden, A. M. Farrington, and P. E. Vincent. PyFR: An open source framework for solving advection-diffusion type problems on streaming architectures using the flux reconstruction approach. *Computer Physics Communications*, 2014.
- [5] Franck Cappello. Fault tolerance in petascale/exascale systems: Current knowledge, challenges and research opportunities. In *International Journal of High Performance Computing Applications*, 2009.
- [6] A. N. Tikhonov and A. A. Samarskii. Homogeneous difference schemes. *USSR Computational Mathematics and Mathematical Physics*, 1962.

- [7] S. V. Patankar. Numerical heat transfer and fluid flow. 1980.
- [8] Timothy J. Barth and Paul O. Frederickson. Higher order solution of the euler equations on unstructured grids using quadratic reconstruction. In *28th Aerospace Sciences Meeting, 1990*, 1990.
- [9] Carl Ollivier-Gooch and Michael Van Altena. A high-order-accurate unstructured mesh finite-volume scheme for the advection-diffusion equation. *Journal of Computational Physics*, 2002.
- [10] Stéphane Louis Clain, Gaspar J. Machado, and Rui M. S. Pereira. A new very high-order finite volume method for the 2D convection diffusion problem on unstructured meshes. In *IV Conferência Nacional em Mecânica dos Fluidos, Termodinâmica e Energia*, 2012.
- [11] X. Nogueira, L. Cueto-Felgueroso, I. Colominas, H. Gómez, F. Navarrina, and M. Casteleiro. On the accuracy of finite volume and discontinuous Galerkin discretizations for compressible flow on unstructured grids. *International Journal for Numerical Methods in Engineering*, 2009.
- [12] Carl F. Ollivier-Gooch. High-order ENO schemes for unstructured meshes based on least-squares reconstruction. In *35th Aerospace Sciences Meeting and Exhibit*, 1997.
- [13] Changqing Hu and Chi Wang Shu. Weighted Essentially Non-oscillatory Schemes on Triangular Meshes. *Journal of Computational Physics*, 1999.
- [14] Alireza Jalali and Carl Ollivier-Gooch. Higher-order unstructured finite volume RANS solution of turbulent compressible flows. *Computers and Fluids*, 2017.
- [15] Alireza Jalali and Carl Ollivier-Gooch. Higher-order unstructured finite volume methods for turbulent aerodynamic flows. In *22nd AIAA Computational Fluid Dynamics Conference*, 2015.
- [16] A. Vasconcelos. *A Very High-Order Finite Volume Method Based on Weighted Least Squares for the Solution of Poisson Equation on Unstructured Grids (MSc thesis)*. 2017.
- [17] F. J. M. Diogo. *A Very High-Order Finite Volume Technique for Convection-Diffusion Problems on Unstructured Grids (MSc thesis)*. 2019.
- [18] C. F. Curtiss and J. O. Hirschfelder. Integration of Stiff Equations. *Proceedings of the National Academy of Sciences*, 1952.
- [19] A. B. Farnell and Peter Henrici. Discrete Variable Methods in Ordinary Differential Equations. *The American Mathematical Monthly*, 1962.
- [20] Ami Harten, Bjorn Engquist, Stanley Osher, and Sukumar R. Chakravarthy. Uniformly high order accurate essentially non-oscillatory schemes, III. *Journal of Computational Physics*, 1987.
- [21] Hester Bijl, Mark H. Carpenter, and Veer N. Vatsa. Time integration schemes for the unsteady navier-stokes equations. In *15th AIAA Computational Fluid Dynamics Conference*, 2001.
- [22] J. R. Cash. On the integration of stiff systems of O.D.E.s using extended backward differentiation formulae. *Numerische Mathematik*, 1980.
- [23] J. R. Cash. The integration of stiff initial value problems in ODEs using modified extended backward differentiation formulae. *Computers and Mathematics with Applications*, 1983.
- [24] G. Psihoyios. A class of implicit advanced step-point methods with a parallel feature for the solution of stiff initial value problems. *Mathematical and Computer Modelling*, 2004.
- [25] S. Deng. *Quadrature formulas in two dimensions*. Dept. of Mathematics and Statistics, UNC at Charlotte, 2010.
- [26] J. E. Akin. *Finite Element Analysis with Error Estimators*. 2005.
- [27] R. S. Hutchinson, Scott A., Shadid, J. N., Tuminaro. *Aztec User's Guide Version 1.1*. Massively Parallel Computing Research Laboratory, Sandia National Laboratories, 1999.